ARL-TR-9607 ● Oct 2022

DEVCOM ARMY RESEARCH LABORATORY

Experimental Investigation of $Yb_2Si_2O_7$ with Molten Calcia-Magnesia-Alumina-Silicate (CMAS) Deposits

by Christopher Louzon, Anindya Ghoshal, and Andrew J Wright

NOTICES

Disclaimers

The findings in this report are not to be construed as an official Department of the Army position unless so designated by other authorized documents.

Citation of manufacturer's or trade names does not constitute an official endorsement or approval of the use thereof.

Destroy this report when it is no longer needed. Do not return it to the originator.

ARL-TR-9607 ● OCT 2022

Experimental Investigation of High-Temperature Interactions of $Yb_2Si_2O_7$ with Molten Calcia-Magnesia-Alumina-Silicate (CMAS) Deposits

Christopher Louzon
SMART Scholar, Brown University

Anindya Ghoshal
DEVCOM Army Research Laboratory

Andrew J Wright
Oak Ridge Associated Universities

REPORT DOCUMENTATION PAGE

Form Approved
OMB No. 0704-0188

1. REPORT DATE *(DD-MM-YYYY)*	2. REPORT TYPE	3. DATES COVERED (From - To)
October 2022	Technical Report	16 May–5 August 2022

4. TITLE AND SUBTITLE
Experimental Investigation of High-Temperature Interactions of $Yb_2Si_2O_7$ with Molten Calcia-Magnesia-Alumina-Silicate (CMAS) Deposits

5a. CONTRACT NUMBER

5b. GRANT NUMBER

5c. PROGRAM ELEMENT NUMBER

6. AUTHOR(S)
Christopher Louzon, Anindya Ghoshal, and Andrew J Wright

5d. PROJECT NUMBER

5e. TASK NUMBER

5f. WORK UNIT NUMBER

7. PERFORMING ORGANIZATION NAME(S) AND ADDRESS(ES)
DEVCOM Army Research Laboratory
ATTN: FCDD-RLW-VA
Aberdeen Proving Ground, MD 21005

8. PERFORMING ORGANIZATION REPORT NUMBER
ARL-TR-9607

9. SPONSORING/MONITORING AGENCY NAME(S) AND ADDRESS(ES)

10. SPONSOR/MONITOR'S ACRONYM(S)

11. SPONSOR/MONITOR'S REPORT NUMBER(S)

12. DISTRIBUTION/AVAILABILITY STATEMENT
Approved for public release: distribution unlimited.

13. SUPPLEMENTARY NOTES
ORCID ID: Anindya Ghoshal, 0000-0001-6338-1224

14. ABSTRACT
Three experimental methods are applied to $Yb_2Si_2O_7$ environmental barrier coating samples to examine coating interactions with calcia-magnesia-alumina-silicate (CMAS) deposits. Thermal cycling and CMAS deposition are performed with an atmospheric burner-rig. Thermal cycling with CMAS loading is performed separately using a box furnace. The contact angle of CMAS as it melts atop a sample is measured using a high-temperature contact-angle measurement system. This testing demonstrates the variety of data achievable from different testing methods. Future work will include a full evaluation of a candidate coating for next-generation gas-turbine engines.

15. SUBJECT TERMS
Mechanical Sciences, Sciences of Extreme Materials, ceramic matrix composites, SiC-SiC, thermal and environmental barrier coating, ytterbium di-silicate, calcia-magnesia-alumina-silicate, CMAS

16. SECURITY CLASSIFICATION OF:			17. LIMITATION OF ABSTRACT	18. NUMBER OF PAGES	19a. NAME OF RESPONSIBLE PERSON
a. REPORT	b. ABSTRACT	c. THIS PAGE			Anindya Ghoshal
Unclassified	Unclassified	Unclassified	UU	25	19b. TELEPHONE NUMBER (Include area code) (410) 278-7358

Standard Form 298 (Rev. 8/98)
Prescribed by ANSI Std. Z39.18

Contents

List of Figures

List of Tables

1. Introduction and Background

Gas-turbine engines in US Army helicopters can be damaged by ingestion of particulates such as sand, ash, and dust. As engine efficiencies have improved, operating temperatures have surpassed the melting point of these particulates. Ingested molten particulates can deposit inside the hot section of the engine. Typically, protective ceramic coatings are sprayed atop the structural materials (e.g., Ni-based superalloys or ceramic matrix composites) in this region of the engine. The deposits, known as calcia-magnesia-alumina-silicates (CMASs), react with and degrade the engine.

A literature review of state-of-the-art ceramic-coating technologies identified $Yb_2Si_2O_7$ as a possible baseline candidate for this study. The CMAS composition, AFRL-02, was developed based on samples retrieved from the field, and this type of CMAS is composed of various minerals.[1]

In many deposit–ceramic interaction studies, only one experimental method is used to qualify an engine materials system. However, there are many test methods available, and it can be difficult to compare results between methods. In this project, a coating ($Yb_2Si_2O_7$) is tested for CMAS interaction using three test methods: atmospheric burner-rig, thermal cycling in box furnace, and contact-angle measurement. A comparison of these test methods is noted.

2. Literature Review

Thermal and environmental barrier coatings have developed over the past 15 years to encompass a variety of materials. Traditional coatings consist of the following layers: substrate (structural material), bondcoat, environmental barrier coatings (EBCs), interlayer, and thermal barrier coatings (TBCs). This multilayer system requires consistent matches of coefficients of thermal expansion between each layer to reduce the potential for thermally induced delamination. The TBC functions to allow the hot section of the engine to operate at temperatures above the melting point of the structural materials. The EBC protects the structural materials from degradation by molten CMAS deposits and steam corrosion.

Barium strontium aluminum silicate (BSAS) was proposed to provide oxidation resistance at operating temperatures (≤1200 °C).[1] As engine temperatures increased above the melting point of sand (~1200 °C), new coatings were needed to provide resistance to degradation from molten CMAS deposits. Yttria-stabilized zirconia, YSZ (7 wt% Y_2O_3 – 93 wt% ZrO_2), was identified as a new standard, demonstrating a robust suite of properties including enhanced CMAS resistance, thermal stability,

and low thermal conductivity.[2] Currently, YSZ is still a common protective ceramic coating used in jet engines. Gadolinium zirconate (GZO) was explored as a potential successor to YSZ or as sacrificial top layer to YSZ. Though GZO demonstrated superior reactivity with CMAS and inhibition of CMAS penetration, its weak mechanical properties make it vulnerable to undesirable cracking.[3,4]

A new approach gained attention: doping these standard coatings to enhance their properties. YSZ doped with Gd or Er cations demonstrated some improved CMA resistance.[5] Some work explored GZO doped with Ti to some success.[6] Another study explored doping YSZ with Al and Ti, using Ti as a sacrificial cation to inhibit the CMAS penetration.[2] Other work included Gd-doped yttrium-aluminum-garnet, known as YAG.[7] Some work explored increasing the yttria content of YSZ.[3] However, none of these coatings succeeded YSZ.

Rare-earth silicates showed promise as EBCs. They also demonstrated excellent phase stability in the high engine operating temperature range. Some of these EBCs, such as Lu_2SiO_5 and Er_2SiO_5, demonstrated secondary phase formation upon reaction with CMAS.[8] $Y_2Si_2O_7$ showed significant cracking due to phase instability in addition to secondary phase formation during CMAS reactions.[9] $Yb_2Si_2O_7$ showed significant secondary phase formation and slower degradation than other compositions.[10] $Er_2Si_2O_7$ behaved similar to $Yb_2Si_2O_7$ with secondary apatite phase formation.[11] Some studies have investigated cerates, tantalates, and other compositions, but these published studies do not examine CMAS resistance.

The compositional possibilities for novel TBCs/EBCs are limited, and the latest research is exploring the potential of high-entropy ceramics for this application. The high-entropy concept manipulates configurational entropy to gain enhanced stability, reduced thermal conductivity, and slower reaction kinetics. In one study, $(La_{0.2}Nd_{0.2}Sm_{0.2}Eu_{0.2}Gd_{0.2})_2Zr_2O_7$ showed a dense reaction layer with rod-shaped crystals and mainly apatite phase formation.[12] Limited cracking occurred in contrast to $La_2Zr_2O_7$.[12] Another composition, $(Y_{0.2}Gd_{0.2}Er_{0.2}Yb_{0.2}Lu_{0.2})_2Zr_2O_7$, demonstrated lower coating recession than GZO, and Y^{3+}-rich and Gd^{3+}-rich secondary phases formed.[13] Medium-entropy ceramics consist of three cations. $(Eu_{0.25}Ho_{0.25}Yb_{0.25}Lu_{0.25})_2SiO_5$ was designed using large cation atomic radii to better resist CMAS corrosion, and little to no cracking was observed.[14] $(Sc_{0.25}Y_{0.25}Er_{0.25}Yb_{0.25})_2Si_2O_7$ showed the potential to form a dense, nonreactive secondary phase layer to inhibit CMAS penetration.[15]

3. Methods

3.1 Samples

$Yb_2Si_2O_7$ powder (Oerlikon-Metco) was plasma-sprayed onto three 1-inch Hexoloy substrate discs coated with Si bondcoat (Oerlikon-Metco). The samples were annealed at 1316 °C for 10 h. Prior to testing, each sample was imaged with an optical microscope. The weight of each sample was recorded. Three thickness measurements were performed, and the average thickness was recorded.

The CMAS formed from molten sand in the combustor is used in this study. The synthetic sand composition is AFRL-02, produced by Powder Technologies Inc. The reported AFRL-02 composition is 34% quartz, 30% gypsum, 17% aplite, 14% dolomite, and 5% salt.[16]

3.2 Atmospheric Burner-Rig/Hot Particulate Ingestion Rig (HPIR)

The sample was mounted 5 inches from the exhaust and moved out of the flame path (Fig. 1). The burner-rig exhaust was set to 1550 °C, using a fuel rate of 8 gal/h, and run for 10 min to allow the system to reach steady-state. A Type-C thermocouple was inserted into the exhaust to approximate the exhaust temperature. CMAS (AFRL-02) was ingested continuously into the flame at a rate of 1 g/min. The sample was moved into the flame for 10 min, then moved out of the flame for 10 min. This cycling was performed for a total of three in/out cycles. Throughout the testing, the temperature of the sample and exhaust was measured using an IR camera and a dual-wavelength pyrometer.

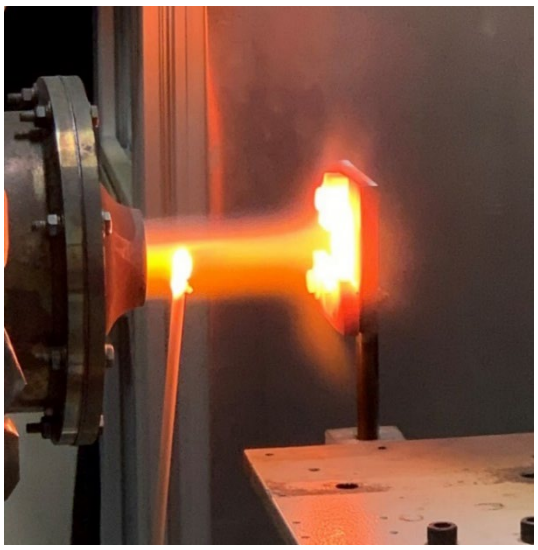

Fig. 1 Burner-rig exhaust for a typical button sample

3.3 Box Furnace Thermal Cycling

A box furnace (KSL-1700X, MTI Corporation, CA) was used for thermal cycling. The furnace cycled from 1350 to 600 °C at a heating/cooling rate of 5 °C/min with a dwell time of 10 min at those two temperatures. This cycling repeated for a total of three dwell times at both temperatures. The upper limit temperature was chosen to approximate the same surface temperature of the sample during burner-rig testing. The lower limit temperature was chosen to simulate the ambient "out-of-flame" temperature of the sample.

3.4 Contact-Angle Measurement

CMAS was mixed with ethanol to create a thick paste, which was then rolled into a 0.19824-g ball 6.042 mm in diameter. The ball was placed in the top center of the sample. The sample was then loaded into high-temperature contact angle measurement hardware with a tube furnace (DataPhysics Instruments) and heated to 1278 °C at a rate of 5 °C/min. The sample was observed using a digital camera. The sample was held at 1278 °C for 30 min, then cooled to room temperature at a rate of 5 °C/min. The instrument software (DataPhysics Instruments) continuously calculated the contact angle during image recording (Fig. 2).

Fig. 2 Contact-angle test measurement setup for a standard sample

3.5 Characterization

All samples were cut and polished to a 1-µm finish according to standard ceramic processing protocols using a diamond saw and a polishing machine (Struers). Samples were suspended in acrylic (SampleKwick, Buehler) prior to polishing. Samples were observed under low vacuum in a scanning electron microscope

(SEM, Hitachi, Japan) in conjunction with energy-dispersive X-ray spectroscopy (EDS, Bruker).

4. Results

The sample masses are noted in Table 1. The burner-rig sample shows the greatest change in sample mass, which can be attributed to a higher loading of CMAS. The sample thicknesses are listed in Table 2. The burner-rig sample showed a thick glass layer on the surface, likely the reason for the increase in thickness. The box-furnace sample thickness increased due to delamination of the ceramic coating. The CMAS glass also contributed to this thickness change. The contact-angle sample thickness growth is likely due to the CMAS layer present on the sample.

Table 1 Mass of samples before/after testing

Sample	Mass before (g)	Mass after (g)	Mass change (g)
Burner rig	5.68070	6.01804	0.33734
Box furnace	5.73452	5.87629	0.14177
Contact angle	5.65475	5.79199	0.22154

Table 2 Thickness of samples before/after testing

Sample	Thickness before (mm)	Thickness after (mm)	Thickness change (mm)
Burner rig	3.50	4.04	0.54
Box furnace	3.55	4.32	0.77
Contact angle	3.45	3.98	0.53

Optical micrographs of the samples demonstrate approximate uniformity before testing, as shown in Fig. 3. After testing, distinct differences are observed. In Fig. 4 (left) the thick glass layer covers the entire sample. In Fig. 4 (middle) the thin glass layer is visible. The delaminated coating areas are fragile and show significant surface cracking. The contact-angle sample in Fig. 4 (right) shows some pitting in the center, possibly due to bubbles in the CMAS glass. A possible cause of these bubbles is the partial decomposition of the minerals in this CMAS during heating and melting.

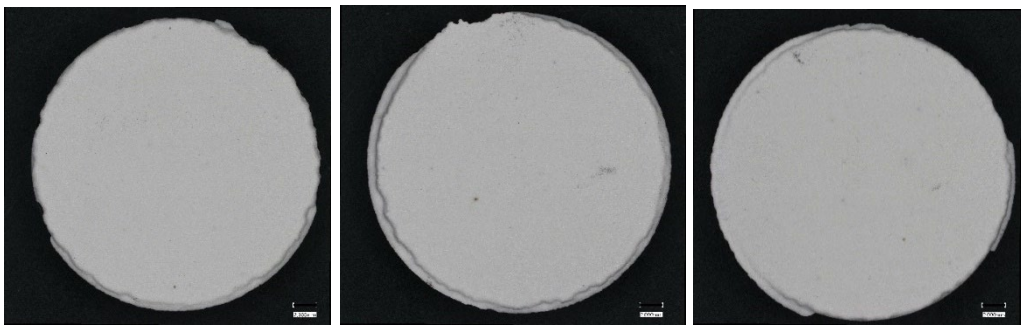

Fig. 3 Optical microscope images of samples prior to testing by (left) burner-rig, (middle) furnace cycling, and (right) contact angle

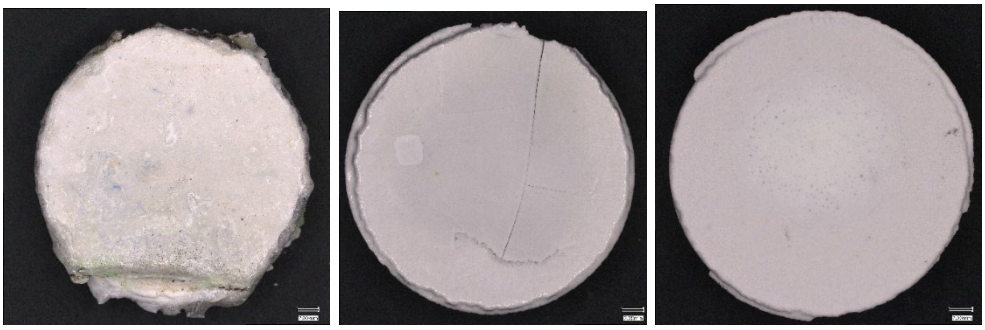

Fig. 4 Optical microscope images of samples after testing by (left) burner-rig, (middle) furnace cycling, and (right) contact angle

4.1 Atmospheric Burner-Rig/HPIR

The burner-rig exhaust and sample temperatures are measured in various ways. The thermocouple placed in the exhaust path failed during testing, and the data could not be retrieved. The IR camera data (Fig. 5) shows that the sample reaches approximately 2100 °F in-flame and cools to below 900 °F out-of-flame.

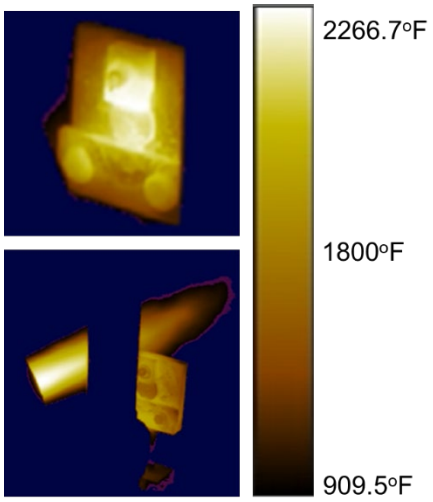

Fig. 5 IR camera images of sample (top, in-flame; bottom, out-of-flame)

The thermal cycling program is shown in Fig. 6. This indicates the in-flame and out-of-flame temperatures. The thermal data from the dual-wavelength pyrometers is presented in Fig. 7. The pyrometers shut down periodically during temperature measurement, so this dataset is incomplete. As noted, the maximum surface temperature reaches 2200 °F.

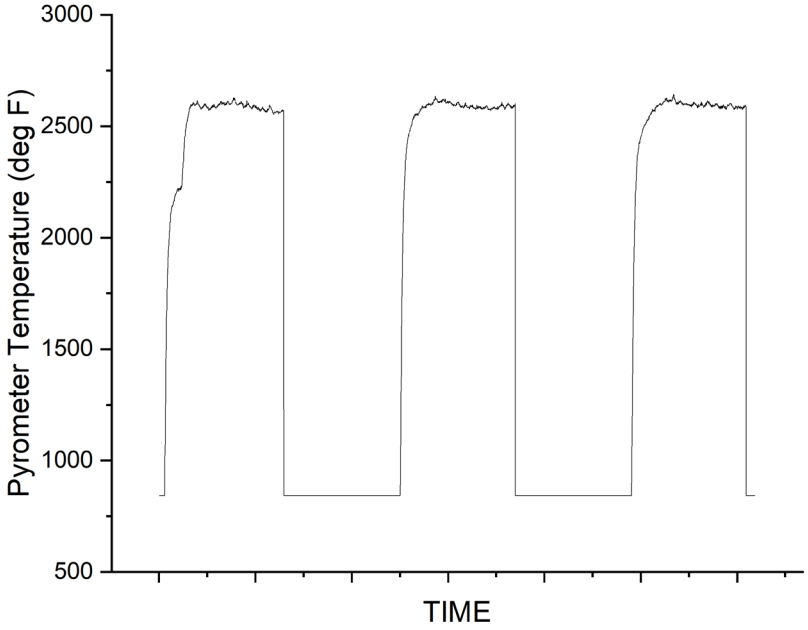

Fig. 6 Burner-rig thermal cycling program

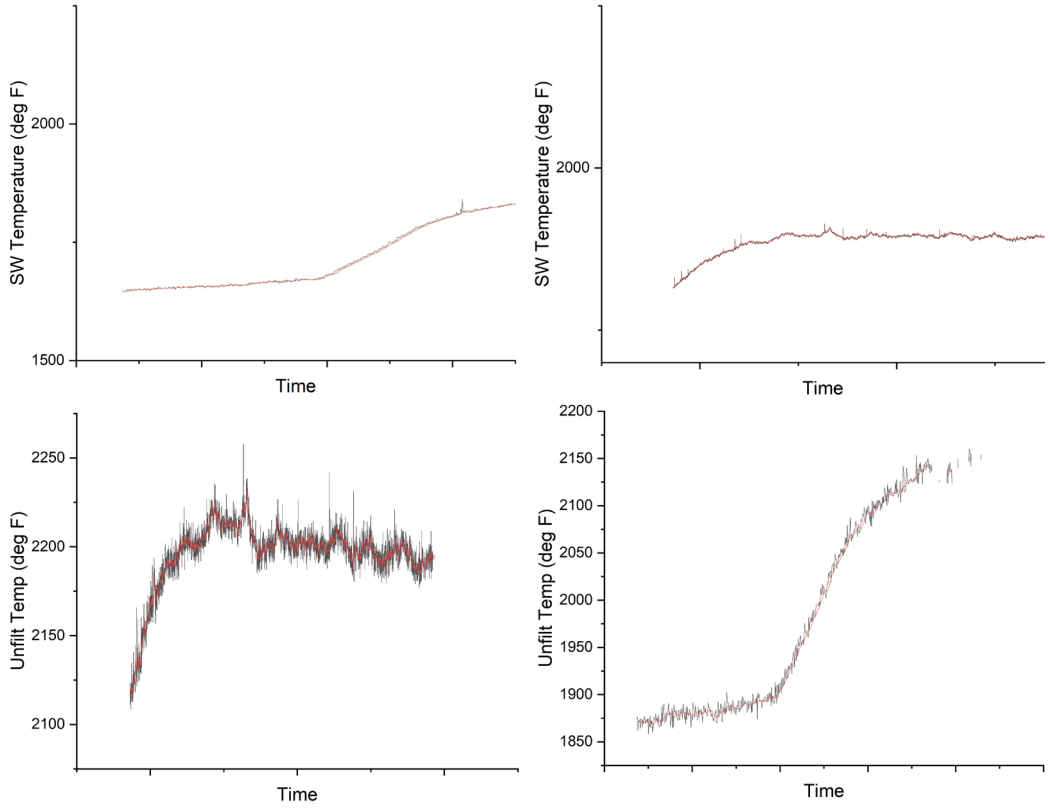

Fig. 7 Thermal data from burner-rig testing (top left) single-wavelength (SW) temperature (Section 1); (top right) SW temperature (Section 2); (bottom left) unfiltered temperature (Section 1); and (bottom right) unfiltered temperature (Section 2)

SEM micrographs and EDS elemental maps of cross sections of all samples post-testing are presented in the following figures.

The SEM micrograph in Fig. 8 (left) shows the layers of the coating system with CMAS. In order from top to bottom, the layers are CMAS glass, $Yb_2Si_2O_7$ coating, Si bondcoat, and Hexoloy substrate. Figure 8 (right) showcases the horizontal delamination of the coating in the sample as well as the vertical cracking that appears to be caused by physical stresses.

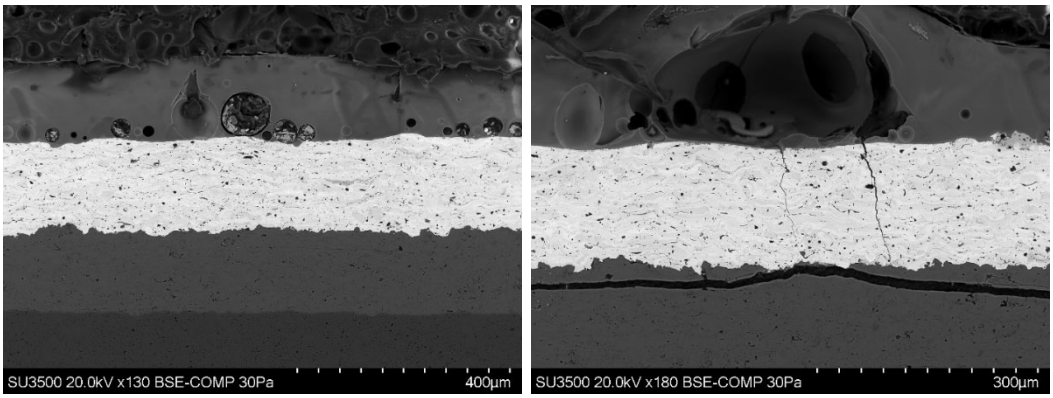

Fig. 8 SEM micrographs of burner-rig sample: CMAS glass layer visible atop coating. (left) Region 1 and (right) Region 2 with visible cracking and delamination.

The EDS maps shown in Fig. 9 suggest that the CMAS dissolves the $Yb_2Si_2O_7$ coating (shown by the presence of Yb in the CMAS melt layer in bottom right) and forms secondary phases rich in Ca (shown by the brighter fragments in the CMAS melt in bottom left).

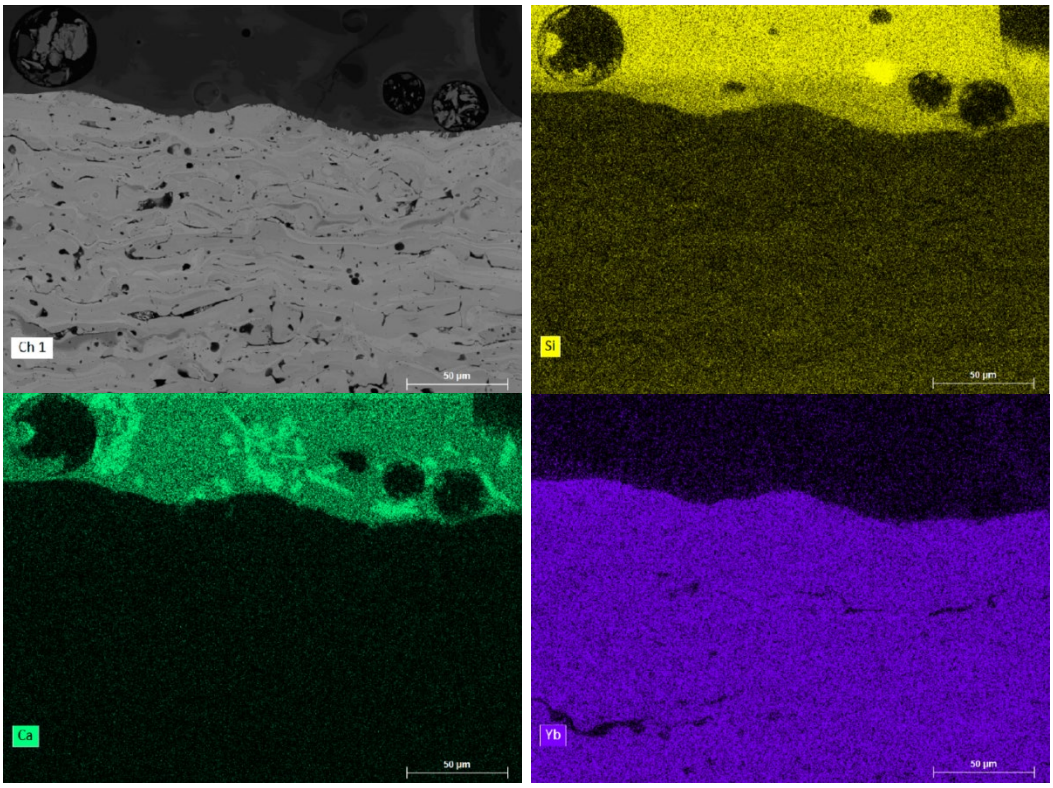

Fig. 9 SEM/EDS maps of burner-rig sample: (top left) SEM micrograph; (top right) Si elemental map; (bottom left) Ca elemental map; and (bottom right) Yb elemental map

4.2 Box-Furnace Thermal Cycling

A SEM micrograph of the reacted sample from box-furnace thermal cycling is shown in Fig. 10. The bondcoat remains attached to the $Yb_2Si_2O_7$ topcoat while fully detaching from the Hexoloy substrate.

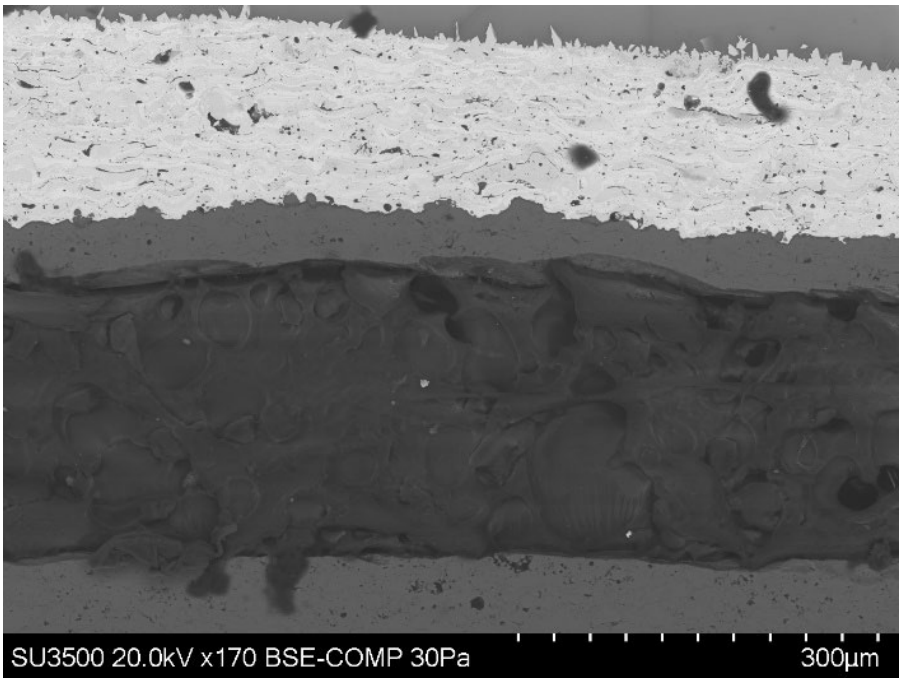

Fig. 10 SEM micrograph of box-furnace sample

EDS elemental mapping of a separate reaction zone on this sample suggests that the bondcoat is fully attached to the EBC topcoat (Fig. 11). The top CMAS layer appears to contain Yb, suggesting that CMAS dissolves the EBC during interaction.

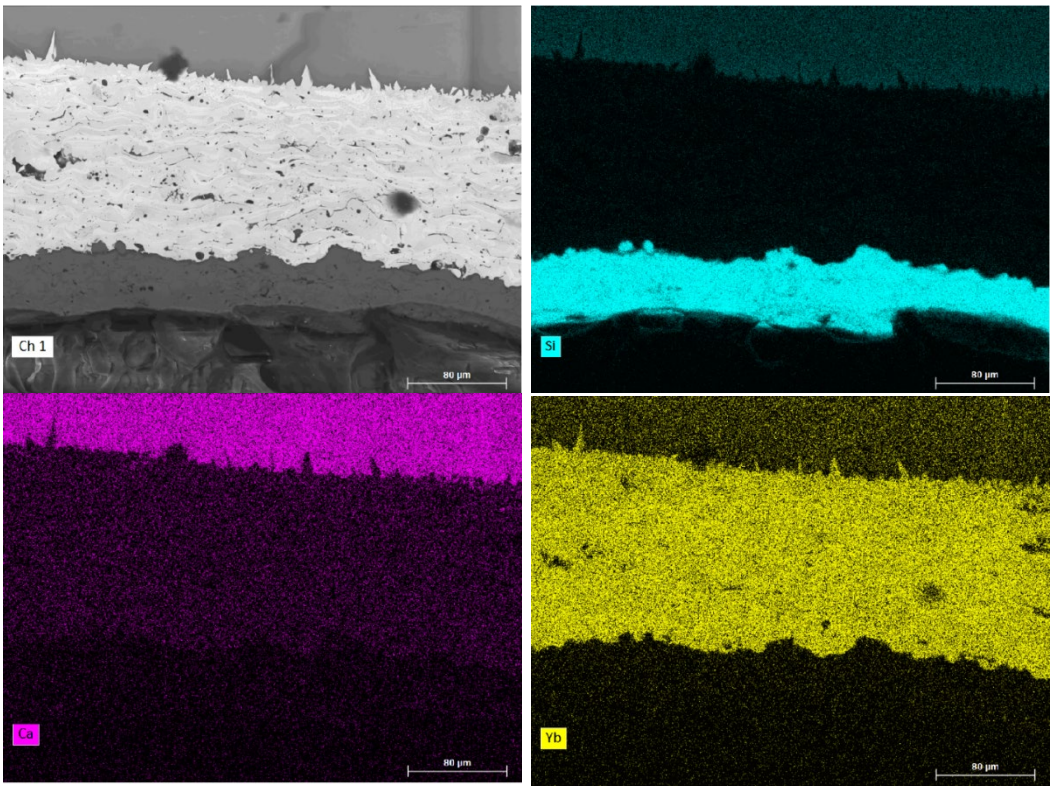

Fig. 11 SEM/EDS maps of box-furnace sample: (top left) SEM micrograph; (top right) Si elemental map; (bottom left) Ca elemental map; and (bottom right) Yb elemental map

4.3 Contact Angle

The spreading of the CMAS glass is visible in the SEM micrograph in Fig. 12 (left). Some continuous vertical cracking is shown through the CMAS and the $Yb_2Si_2O_7$ layers (Fig. 12, right).

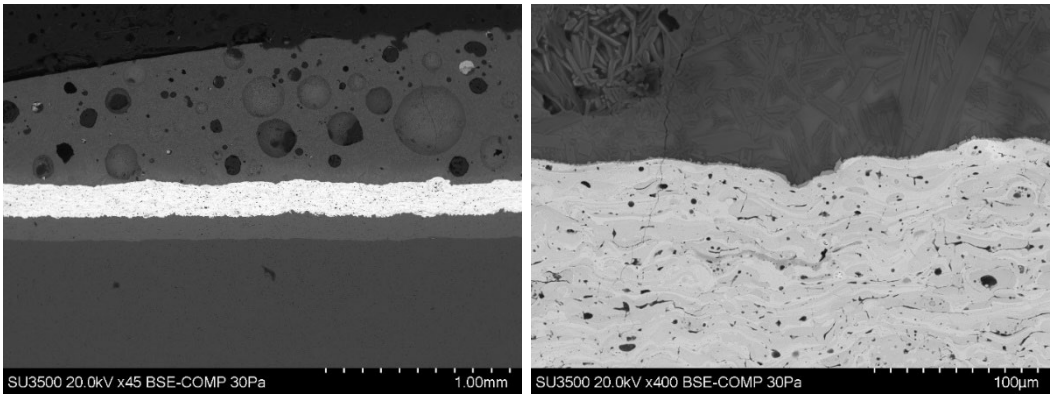

Fig. 12 SEM micrographs of box-furnace sample: (left) Post-reaction system. Layers (top to bottom) visible are CMAS glass, $Yb_2Si_2O_7$ coating, Si bondcoat, and Hexoloy substrate. (right) Higher-magnification image of coating/CMAS interface.

EDS elemental mapping of the CMAS/EBC interface suggests rod-like crystalline phase formation within the CMAS glass melt (Fig. 13). The upper layer of the EBC appears to have pockets rich in Si. There is a uniform penetration boundary, noted by the distinct area rich in Yb/Si at the bottom of the sample.

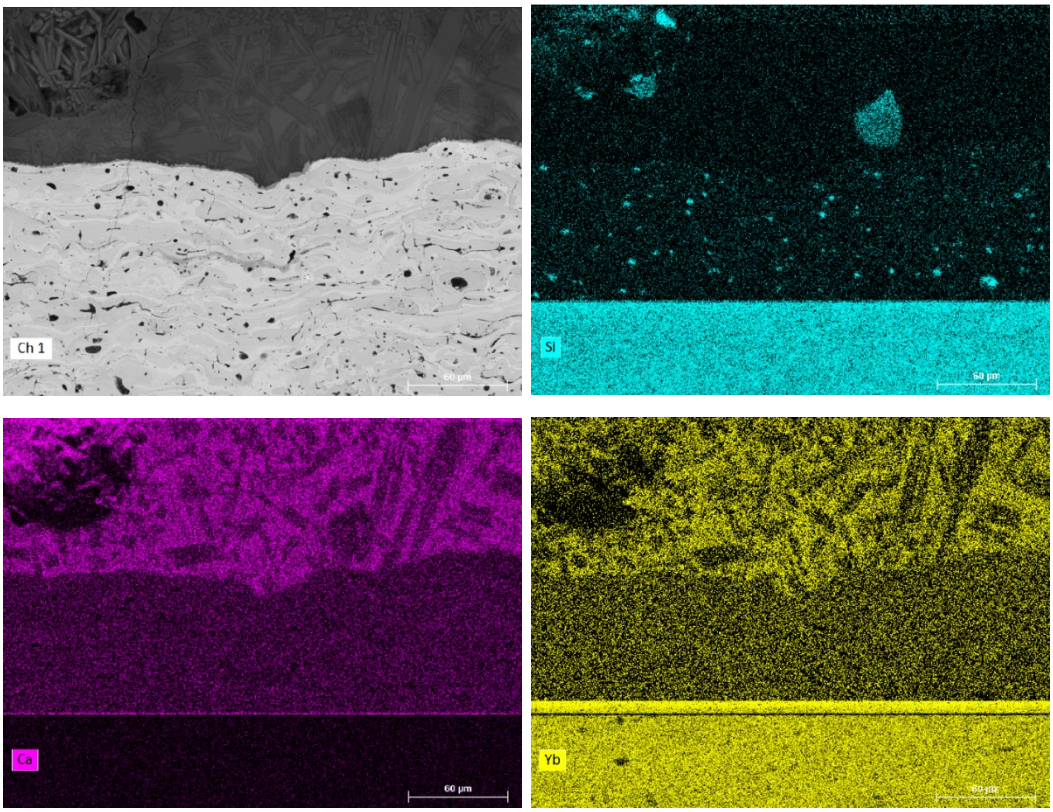

Fig. 13 SEM/EDS maps of contact-angle sample: (top left) SEM micrograph; (top right) Si elemental map; (bottom left) Ca elemental map; and (bottom right) Yb elemental map

5. Discussion

This study compares various evaluation methods used to examine the interactions of CMAS with ceramic coatings. Optical microscope imaging details the macroscopic effects of various testing on the sample. The burner-rig exhaust deposits a thick layer of glass across the entire sample. The thermal cycling sample is covered in a thinner layer of glass. The contact-angle sample has a thicker glass layer in the center of the sample.

The burner-rig has many variables and shows some limits in accurately regulating and monitoring operating conditions. Its greatest advantage is its achievement of conditions that closely approach those of a gas-turbine engine. The burner-rig also allows for ingestion and deposition of CMAS particulates. This type of testing is cheaper and easier to implement than full-engine testing.

The box-furnace test allows for well-controlled thermal testing. However, this does not accurately reflect the inherent thermal gradient present in gas-turbine engines. Furnace testing also is limited to slow heating/cooling rates, which reduce the effectiveness of thermal cycling.

The contact-angle measurement, when shown in conjunction with other experimental data, is quite insightful with melting behavior. Degradation depends on agent loading, which is typically only controlled initially at room temperature for this test. As the corrosive agent melts and spreads, the loading across the surface of the sample varies and this affects the interactions that occur. The testing techniques are compared in Table 3.

Table 3 Comparison of three CMAS-testing techniques

	Atmospheric burner-rig	Box-furnace thermal cycling	Contact-angle measurement
Benefits	• Simulates engine conditions (pressure, temperature, and velocity) • Allows for particle ingestion/deposition	• Highly controlled • Can provide clear information about chemical reactions • Cheap • Easy	• Describes wetting glass on sample surface
Limitations	• Many variables • Difficult to monitor testing conditions accurately	• Unrealistic • Limited by speed of heating/cooling for cycling	• No chemical information • Does not account for particles' physical impact on coating

The degradation of the glass is influenced by the amount, thickness, composition, and porosity of the glass melt. The CMAS degradation is visible in each sample. EDS mapping shows consistent dissolution of the $Yb_2Si_2O_7$ layer into the melt. Some secondary phase formation is visible in the melt, but additional phase identification studies are needed to confirm what phases are present.

6. Conclusions

Three CMAS-testing methods were employed to evaluate a state-of-the-art ceramic coating ($Yb_2Si_2O_7$). Comparisons were drawn between each test method.

Future work on this project will involve developing and spraying a new ceramic composition. This novel coating would be tested using these three methods to determine its viability. The emissivity of the sample and its evolution during CMAS deposition are critical to recording burner-rig thermal data. This property varies among samples. Various methods could be used to measure this, including black-

body furnace testing or high-temperature Fourier transform infrared spectroscopy. Further characterization of the sample–CMAS interaction could be performed by mixing CMAS and $Yb_2Si_2O_7$ powder and performing a diffraction phase identification study via heating in situ.

7. References

1. Grant KM, Krämer S, Löfvander JPA, Levi CG. CMAS degradation of environmental barrier coatings. Surface and Coatings Technology. 2007;202(4):653–657. doi:10.1016/j.surfcoat.2007.06.045.

2. Drexler JM, Shinoda K, Ortiz AL, Li D, Vasiliev AL, Gledhill AD, Sampath S, Padture NP. Air-plasma-sprayed thermal barrier coatings that are resistant to high-temperature attack by glassy deposits. Acta Materialia. 2010;58(20):6835–6844. doi:10.1016/j.actamat.2010.09.013.

3. Morelli S, Bursich S, Testa V, Bolelli G, Miccichè A, Lusvarghi L. CMAS corrosion and thermal cycling fatigue resistance of alternative thermal barrier coating materials and architectures: a comparative evaluation. Surface and Coatings Technology. 2022;439:128433. doi:10.1016/j.surfcoat.2022.128433.

4. Müller D, Hess K-U, Kueppers U, Lokachari S, Dingwell DB, Wolf G, Rokicki P, Nowotnik A. Rheological and chemical interaction between volcanic ash and thermal barrier coatings. Surface and Coatings Technology. 2021;412:127049. doi:10.1016/j.surfcoat.2021.127049.

5. Xia J, Yang L, Wu RT, Zhou YC, Zhang L, Yin BB, Wei YG. On the resistance of rare earth oxide-doped YSZ to high temperature volcanic ash attack. Surface and Coatings Technology. 2016;307:534–541. doi:10.1016/j.surfcoat.2016.09.033.

6. Ponnilavan V, Aravind A, Ezhilan M, Kannan S. Titanium substitution in $Gd_2Zr_2O_7$ for thermal barrier coating applications. Ceramics International. 2019;45(13):16450–16457. doi:10.1016/j.ceramint.2019.05.176.

7. Sun S, Xue Z, He W, He J, Li Q, Guo H. Corrosion resistant plasma sprayed $(Y_{0.8}Gd_{0.2})_3Al_5O_{12}$/YSZ thermal barrier coatings towards molten calcium-magnesium-alumina-silicate. Ceramics International. 2019;45(7, Part A):8138–8144. doi:10.1016/j.ceramint.2019.01.114.

8. El Shafei K, Al Nasiri N. Corrosion behavior of rare-earth monosilicates in CMAS exposure. Corrosion Science. 2022;202:110312. doi:10.1016/j.corsci.2022.110312.

9. Poerschke DL, Shaw JH, Verma N, Zok FW, Levi CG. Interaction of yttrium disilicate environmental barrier coatings with calcium-magnesium-iron alumino-silicate melts. Acta Materialia. 2018;145:451–461. doi:10.1016/j.actamat.2017.12.004.

10. Zhao H, Richards BT, Levi CG, Wadley HNG. Molten silicate reactions with plasma sprayed ytterbium silicate coatings. Surface and Coatings Technology. 2016;288:151–162. doi:10.1016/j.surfcoat.2015.12.053.

11. Kim S-H, Fisher CAJ, Nagashima N, Matsushita Y, Jang B-K. Reaction between environmental barrier coatings material $Er_2Si_2O_7$ and a calcia-magnesia-alumina-silica melt. Ceramics International. 2022;48(12):17369–17375. doi:10.1016/j.ceramint.2022.03.001.

12. Tu T-Z, Liu J-X, Zhou L, Liang Y, Zhang G-J. Graceful behavior during CMAS corrosion of a high-entropy rare-earth zirconate for thermal barrier coating material. Journal of the European Ceramic Society. 2022;42(2):649–657. doi:10.1016/j.jeurceramsoc.2021.10.022.

13. Deng S, He G, Yang Z, Wang J, Li J, Jiang L. Calcium-magnesium-alumina-silicate (CMAS) resistant high entropy ceramic $(Y_{0.2}Gd_{0.2}Er_{0.2}Yb_{0.2}Lu_{0.2})_2Zr_2O_7$ for thermal barrier coatings. Journal of Materials Science & Technology. 2022;107:259–265. doi:10.1016/j.jmst.2021.07.053.

14. Chen Z, Tian Z, Zheng L, Ming K, Ren X, Wang J, Li B. $(Ho_{0.25}Lu_{0.25}Yb_{0.25}Eu_{0.25})_2SiO_5$ high-entropy ceramic with low thermal conductivity, tunable thermal expansion coefficient, and excellent resistance to CMAS corrosion. J Adv Ceram. 2022;11(8):1279–1293. doi:10.1007/s40145-022-0609-z.

15. Wang X, Cheng M, Xiao G, Wang C, Qiao R, Zhang F, Bai Y, Li Y, Wu Y, Wang Z. Preparation and corrosion resistance of high-entropy disilicate $(Y_{0.25}Yb_{0.25}Er_{0.25}Sc_{0.25})_2Si_2O_7$ ceramics. Corrosion Science. 2021;192:109786. doi:10.1016/j.corsci.2021.109786.

16. Powder Technology Inc. AFRL 02 test dust. https://www.powdertechnologyinc.com/product/afrl-02-test-dust/.

List of Symbols, Abbreviations, and Acronyms

Al	aluminum
BSAS	barium-strontium-aluminum-silicate
CMAS	calcia-magnesia-alumina-silicate
EBC	environment barrier coating
EDS	energy-dispersive X-ray spectroscopy
Er	erbium
Eu	europium
Gd	gadolinium
GZO	gadolinium zirconate
Ho	homium
HPIR	hot particulate ingestion rig
IR	infrared
La	lanthanum
Lu	lutetium
Nd	neodymium
Ni	nickel
Sc	scandium
SEM	scanning electron microscope
Si	silicon
Sm	samarium
SW	single wavelength
TBC	thermal barrier coating
Ti	titanium
Y	yttrium
YAG	yttrium-aluminum-garnet
Yb	ytterbium

YSZ	yttria-stabilized zirconia
Zr	zirconium

1 (PDF)	DEFENSE TECHNICAL INFORMATION CTR DTIC OCA
1 (PDF)	DEVCOM ARL FCDD RLD DCI TECH LIB
2 (PDF)	DEVCOM ARL FCDD RLW VA A GHOSHAL A WRIGHT
1 (PDF)	BROWN UNIVERSITY C LOUZON